


RESEARCH ARTICLE OPEN ACCESS

Breaking the Bottleneck in Limit of Detection of Surface Refractive Index Sensing by Harnessing Meta-Waveguide Microring Resonators

Wanxin Li¹ | Jiewen Li¹ | Rui Li¹ | Gina Jinna Chen² | Perry Ping Shum² | Yi Zou³ | Ray T. Chen⁴  | Yongkang Dong¹ | Xiaochuan Xu¹

¹National Key Laboratory of Laser Spatial Information, Guangdong Provincial Key Laboratory of Integrated Photonic-Electronic Chip, Guangdong Provincial Key Laboratory of Aerospace Communication and Networking Technology, Harbin Institute of Technology, Harbin Institute of Technology campus, Xili University Town, Shenzhen, Guangdong, China | ²State Key Laboratory of Optical Fiber and Cable Manufacture Technology, Guangdong Key Laboratory of Integrated Optoelectronics Intellisense, Department of EEE, Southern University of Science and Technology, Shenzhen, China | ³School of Information Science and Technology, ShanghaiTech University, Shanghai, China | ⁴Department of Electrical and Computer Engineering, The University of Texas at Austin, Austin, Texas, USA

Correspondence: Yi Zou (zouyi@shanghaitech.edu.cn) | Yongkang Dong (dongyk@hit.edu.cn) | Xiaochuan Xu (xuxiaochuan@hit.edu.cn)

Received: 2 February 2026 | **Revised:** 5 April 2026 | **Accepted:** 7 April 2026

Keywords: meta-waveguide microrings | mode splitting | ultra-sensitive self-referenced sensing

ABSTRACT

Pushing sensor sensitivity to the extreme remains a central pursuit in sensing research. However, the limit of detection (LOD) is ultimately limited by the trade-off between intrinsic sensitivity and noise: improvements in sensitivity often introduce higher noise, yielding only marginal gains in LOD. Here, we leverage mode splitting in meta-waveguide microring resonators (MWMRs)—a typically overlooked phenomenon—to suppress drift-induced bias and noise without sacrificing interfacial refractive-index sensitivity. This approach reduces baseline drift to just 4.6 fm/min during representative measurements, enabling quantitative detection of ultra-weak surface perturbations. The sensing performance is validated through the streptavidin-biotin interaction, achieving reliable detection of 0.01 pg/mL streptavidin with a blank reference and a splitting noise of 1.3 pm. This reflection-induced mode splitting framework breaks the longstanding LOD bottleneck in surface refractometric sensing and establishes MWMRs as a robust, drift-immune platform for ultra-sensitive optical interrogation.

1 | Introduction

Detecting analytes at ultra-low concentrations is critical for applications including sub-picomolar biomarker quantification, single-pathogen identification, and contaminant monitoring in complex environments [1]. These demands have driven ongoing efforts to improve the limit of detection (LOD), defined as the lowest analyte concentration reliably measurable [2]. On-chip microring resonators, characterized by their compact footprint, have emerged as promising sensing platforms [3–9]. However, their sensitivity is often insufficient as the majority of the

optical field is confined within the waveguide core, resulting in weak interactions with surrounding analytes. Incorporating nanostructures into microrings, such as slot waveguides [10, 11], one-dimensional photonic crystal waveguides [12, 13], and meta-waveguides [14–17], opens a new avenue to break the sensitivity limit imposed by conventional guided-wave mechanisms. Despite significant advances in sensitivity, the improvement in LOD remains marginal, as sensitivity-enhanced sensors generally increase susceptibility to environmental disturbances, frequently resulting in the deterioration of LOD. Therefore, overcoming the sensitivity-noise constraint plays a key role in the detection of

This is an open access article under the terms of the [Creative Commons Attribution](https://creativecommons.org/licenses/by/4.0/) License, which permits use, distribution and reproduction in any medium, provided the original work is properly cited.

© 2026 The Author(s). *Advanced Science* published by Wiley-VCH GmbH

extremely refractive-index perturbations. While the macroscopic noise, such as temperature fluctuations and vibrations, can be effectively suppressed by introducing reference channels [7, 18], noise arising from micro- or nanoscale regions remains difficult to mitigate and is particularly critical for detecting individual particles and surface binding dynamics.

In this work, we attempt to address this issue by exploring the mode splitting in meta-waveguide microrings (MWMRs). Mode splitting typically arises from mutual coupling between clockwise (CW) and counterclockwise (CCW) modes in microrings, induced by reflective elements, such as sidewall roughness [19], scatterers [20–22], and periodic structures [23–28], which lift mode degeneracy. It has been intensively investigated as a self-referenced sensing architecture, demonstrating a remarkable ability to detect regional tiny refractive perturbations, such as a single particle or virus [20, 29] due to its inherent noise immunity. However, these approaches are not always beneficial for sensing performance (see Section S1). Accordingly, meta-waveguides are adopted as a platform that enables controlled residual reflection while preserving low optical loss and strong field overlap with the sensing medium. While a meta-waveguide is typically treated as a homogeneous uniaxial crystal [30] without reflection according to Effective Medium Theory (EMT), our recent findings reveal that this approximation is not universally applicable, particularly in resonant configurations [23]. In the practical finite periodic structure considered here, weak internal reflection arises from the finite-length meta-waveguide section (see Section S2 and Figure S1). In the microring, cavity loss and the finite Q factor further impose a finite effective interaction length, so that this internal reflection acts as the back-coupling pathway between the CW and CCW modes, giving rise to mode splitting that can be leveraged for sensitive, low-noise interrogation [31–33]. Building on this concept, we harness mode-splitting-based MWMRs for self-referenced surface sensing. Interfacial refractive-index variations modulate the internal reflection and consequently alter mode splitting, enabling quantitative and stable detection of ultra-weak surface perturbations. This reflection-induced mode splitting approach offers inherent stability and effectively decouples surface-specific signals from environmental noise, positioning MWMRs as a robust photonic platform for high-precision, surface-selective sensing.

2 | Results

2.1 | The Origination of Mode Splitting in MWMRs

The proposed structure is a classic all-pass MWMR, consisting of an MWMR side-coupled to a meta bus waveguide, as shown in Figure 1A. The period (Λ) of the meta-waveguide is 300 nm, which is sufficiently small to prevent diffraction ($\Lambda < \lambda_0/2n_{\text{eff}}$) [30]. The circularly arranged trapezoidal silicon pillars are adopted to minimize the intrinsic loss of the MWMR, while the meta bus waveguide is constructed with rectangular silicon pillars [16]. The gap (g) between the meta bus waveguide and the MWMR is optimized for critical coupling. In this configuration, the reflection response to interfacial refractive-index variations is modeled using a three-layer stack (silicon/cladding/surface layer, as shown in Figure 1B), with layer indices estimated by

a field-weighted effective-index method [34]. The electric field distributions of the transverse-electric (TE) mode of each layer are simulated by the finite element method (FEM) and depicted in the insets of Figure 1B. In practical sensing scenarios, the surface layer could be composite films such as functional coatings, protein probes, and blocking layers, as interfaces typically require sequential modifications before interacting with analytes. Without loss of generality, we model the surface film as a 10 nm-thick uniform layer with refractive index (n) varying with material composition and molecular density [35]. In the simulation, the refractive index n is varied from 1.35 to 1.59, covering the range of typical organic and biomolecular films, including Bovine Serum Albumin (BSA, $n = 1.47$ [35]) and biotin–streptavidin complex ($n = 1.502$ [36]). Figure 1C shows the red-shifted reflectance spectra (R) of the surface-layer-covered meta-waveguide, obtained from a transfer-matrix-based equivalent-reflection model of the finite periodic section (see Section S3 and Figure S2). The reflectance spectra are periodic functions of wavelength, with the peak reflectance reaching a maximum at $n = 1.35$ and gradually decreasing as the index contrast between materials diminishes. The residual reflection in the MWMR gives rise to mode splitting by lifting the degeneracy of CW/CCW modes. Consequently, Figure 1D presents the field distributions (H_z) of the two split modes, with the inset magnifying their distinct spatial profiles.

Transmission spectra (T) of the MWMR, derived by extending this equivalent-reflection model to the coupled microring, where it serves as an effective phenomenological description of the CW–CCW coupling underlying mode splitting (see Section S4 and Figure S3). Figure 2A shows a typical mode splitting spectrum and the corresponding internal reflection, estimated by the aforementioned meta-waveguide model. The amount of mode splitting ($\Delta\lambda_s$), defined as $\lambda_+ - \lambda_-$, is proportional to the strength of the internal reflection [21]. Due to the reflection-induced wavelength-dependent loss, the split modes exhibit different quality factors (Q) [20]. Figure 2B illustrates the evolution of the internal reflection within the meta-waveguide induced by variations in the refractive index of the surface layer. The black (λ_-) and blue (λ_+) curves represent the trajectories of the two resonant wavelengths depicted in Figure 2A, respectively. The corresponding spectra are shown in the right insets of Figure 2B. As n initially increases, $\Delta\lambda_s$ decreases, as illustrated in insets (i)–(v). At $n = 1.436$, the splitting becomes indistinguishable due to the limited Q factor, as shown in inset (vi), where the reflection intensity is approximately 0.09. With a further increase in n , the unresolved resonances in inset (vii) exhibit different Q factors and extinction ratios compared to inset (vi), indicating mode broadening in this region [37]. At $n = 1.444$, the reflection drops to zero, and the resonance transitions to an unsplit state, as illustrated in inset (viii). Beyond the zero-reflection point, unresolvable splitting reappears (insets (ix)–(x)). At $n = 1.448$, mode splitting re-emerges with a splitting of 71 pm, and its strength continues to grow with increasing n , as depicted in insets (xi)–(xv). Figure 2C summarizes the quantified $\Delta\lambda_s$, identifying three regions: decreasing, unsplitting, and increasing. An extended refractive-index range is used in the simulation to capture the full evolution of the mode-splitting behavior, while the experiments probe only a small perturbation within the relevant regime. The unsplitting region includes both the unresolvable splitting and zero-reflection-induced nonsplitting states. The decreasing regime is analyzed as a representative case to elucidate the sensing characteristics. Because the splitting

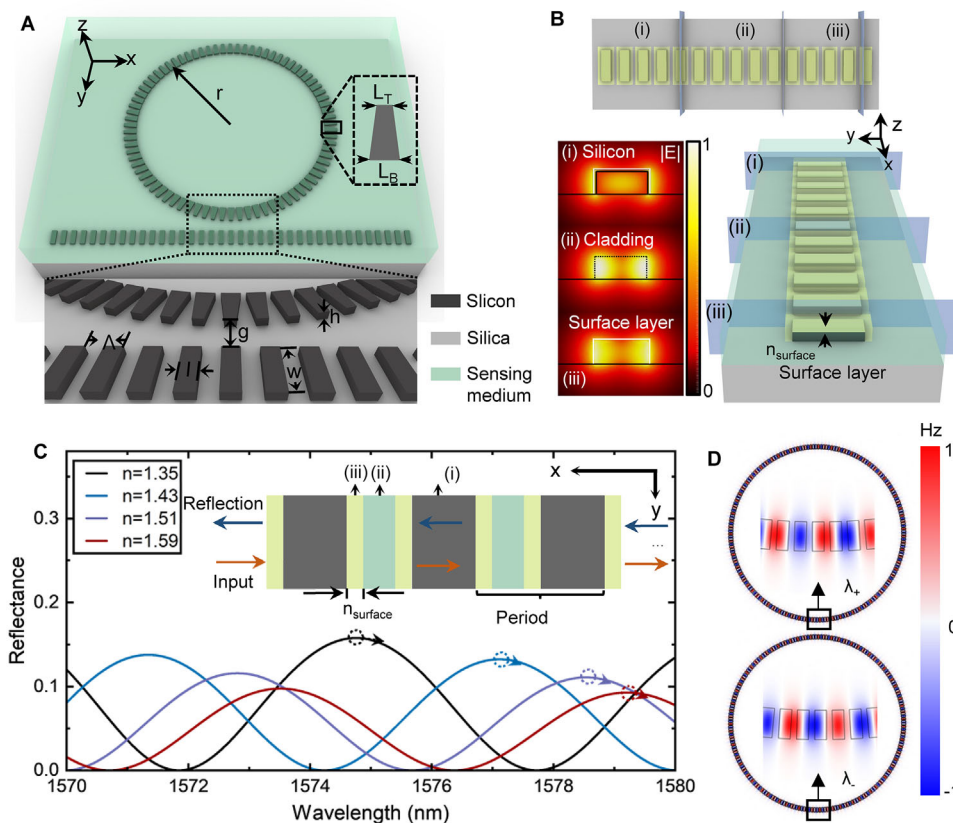


FIGURE 1 | Structure and reflection origin of the MWMR. (A) Schematic of a meta-waveguide side-coupled to an MWMR, showing the side-coupled configuration used for reflection modeling. Parameters of the meta-structure: $L_B = 240$ nm, $L_T = 160$ nm, $r = 10$ μ m, $g = 500$ nm, $h = 220$ nm, $w = 500$ nm, $l = 180$ nm. (B) Electric field distributions of the silicon (i), cladding (ii), and surface-layer (iii) segments. Top inset: top-view of the meta-waveguide. (C) Red-shifted reflectance spectra of the meta-waveguide under varying surface-layer refractive indices. Inset: three-layer-stack model used in reflection simulation. (D) Magnetic field (H_z) distributions of the two split modes, with inset magnifying their distinct spatial profiles.

response is not strictly linear, the surface sensitivity is expressed as a range of 10–15 nm/RIU. Within the same regime, λ_+ and λ_- exhibit stronger surface-induced shifts of 111 and 123 nm/RIU, respectively. To assess practical relevance, the bulk sensitivity is also calculated to evaluate the response to spatially homogeneous refractive-index variations, such as temperature fluctuations, and other non-local background changes. As shown in the inset of Figure 2C, variation of the bulk refractive index induces linear shifts of λ_+ and λ_- (552 and 554 nm nm/RIU), whereas $\Delta\lambda_s$ remains nearly invariant (-1.7 nm/RIU). These results indicate that, although λ_{\pm} and $\Delta\lambda_s$ both respond to surface perturbations, $\Delta\lambda_s$ remains insensitive to bulk variations, establishing it as a stable and reliable sensor for surface-specific sensing. In contrast, the pronounced bulk sensitivity of λ_{\pm} implies that weak surface signals can be easily masked by background-index fluctuations, whereas $\Delta\lambda_s$ effectively isolates the interfacial response and ensures quantitative accuracy even under varying environmental conditions.

2.2 | Noise-Resilient Optical Response Enabled by Mode Splitting in MWMRs

To assess the optical performance and stability of the proposed mode splitting-based MWMR, the fabricated device and experimental setup are shown in Figure 3. Figure 3A shows scanning

electron microscopy (SEM) images of the fabricated MWMR. The detailed fabrication process is described in the Materials and Methods section. The insets of Figure 3A illustrate the coupling region (i) and the adiabatic mode converter (ii). The converters are placed at both ends of the meta bus waveguide to facilitate mode conversion between the fundamental mode of the silicon strip waveguide and that of the meta bus waveguide. The fabricated MWMR is encapsulated in a customized microfluidic package and measured with an in-house automated testing system (see Materials and Methods section, Section S5 and Figure S4), as illustrated in Figure 3B,C. Figure 3D shows the transmission spectrum of the MWMR exhibiting mode splitting when immersed in phosphate-buffered saline (PBS) buffer. The mode splitting occurs near 1530 nm with $\Delta\lambda_s$ of 515 pm. This measurement establishes a spectral reference for subsequent sensing analyses.

The bulk refractometric sensitivity (S) of the MWMR is quantified using NaCl solutions with defined refractive indices. The resonance shifts are linearly fitted against refractive-index variations, as summarized in Figure 4A. The fitted slopes are 351 nm/RIU for λ_+ , 353 nm/RIU for λ_- , and -1.35 nm/RIU for $\Delta\lambda_s$, with error bars representing standard deviations (σ). Figure 4B shows the normalized spectral responses, and the inset compares the baseline noise of λ_+ , λ_- , and $\Delta\lambda_s$ (13 pm, 16.1 pm, and 5.7 pm, respectively). The LOD, calculated as $3\sigma/S$, is determined to

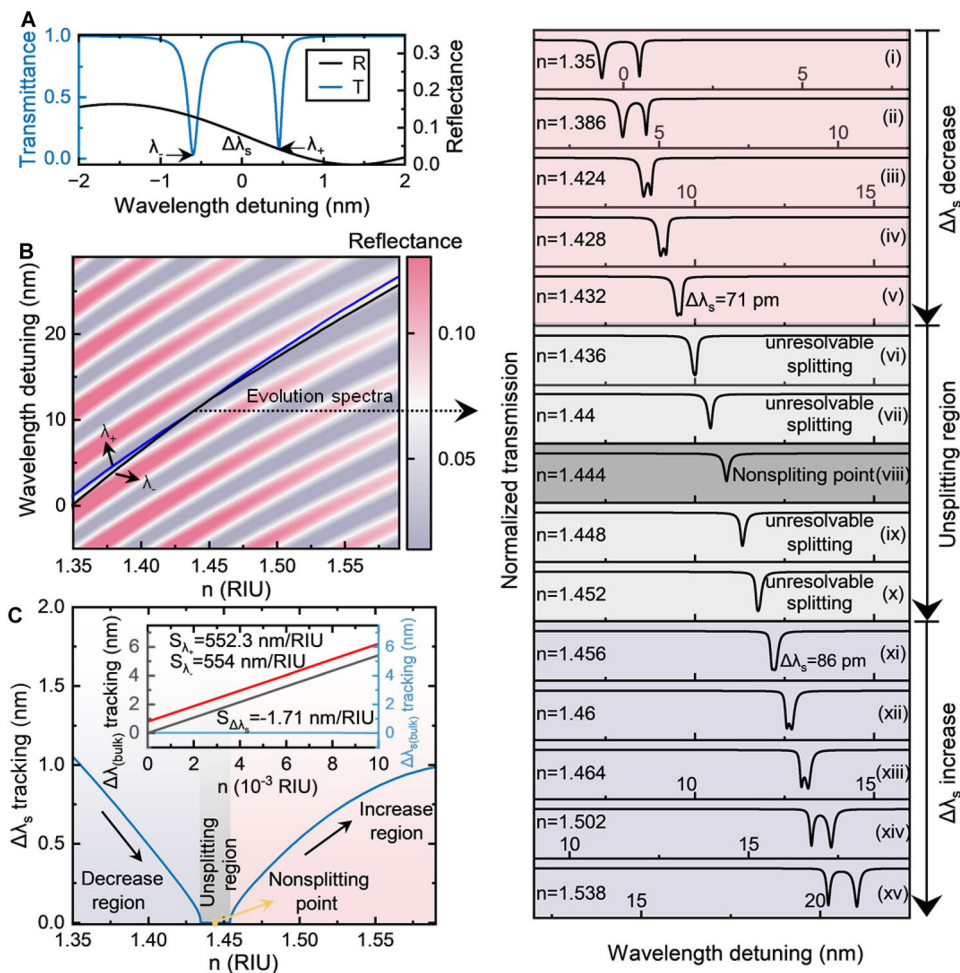


FIGURE 2 | Theoretical evolution of mode splitting with surface index variation. (A) Simulated transmittance and reflectance spectra of the surface-layer-covered MWMR at $n = 1.35$. (B) Black (λ_-) and blue (λ_+) curves trace the trajectories of the two resonant wavelengths in (A); right insets show the corresponding spectral evolution. (C) Quantified $\Delta\lambda_s$ variations with increasing n , identifying three regions—decreasing, unsplitting, and increasing—with inset showing the bulk sensitivities of λ_- , λ_+ , and $\Delta\lambda_s$.

be 9.82×10^{-5} RIU (details in Section S6). These results agree well with the simulation, confirming that $\Delta\lambda_s$ is insensitive to homogeneous bulk-index variations and thus exhibits intrinsic immunity to such perturbations.

The temporal stability of the MWMR is evaluated by analyzing its baseline drift, which is a deterministic factor for achieving an ultra-low LOD [38]. Baseline drift must be kept small enough compared with the biomolecule binding signals. This drift can result from factors such as temperature differences between two solutions and surface oxidation, which contribute to non-negligible signal interferences [36]. Therefore, precise and costly environmental controls are often necessary for conventional sensors to stabilize the sensing system. To demonstrate the effectiveness of the proposed self-referenced sensor, the spectral responses are continuously monitored for 2000 s while the device is immersed in PBS buffer after the 3-aminopropyl triethoxysilane (APTES) monolayer modification (see Materials and Methods), as shown in Figure 4C. Both λ_+ and λ_- exhibit significant red-drift originating from the aforementioned factors at comparable rates (2.88 pm/min and 2.89 pm/min, respectively; statistical analysis can be found in Section S7), whereas $\Delta\lambda_s$ remains stable

with a drift of merely 4.6 fm/min, which is three orders of magnitude lower than the wavelength-shift based interrogation method. This performance is also comparable to that of commercial instruments, such as the Biacore 1 series model, which employs a microfluidic parallel reference channel to suppress blank drift to less than 0.003 RU/min (= 3 fm/min) [39]. The temperature sensitivity of the mode splitting-based MWMR is evaluated under varying environmental conditions, as shown in Figure 4D,E. The high thermo-optic coefficient of silicon ($1.86 \times 10^{-4}/\text{K}$) [40] makes silicon-based devices intrinsically sensitive to thermal perturbations. Accordingly, both resonances of the mode splitting doublet are red-shifted as the temperature increases from 20°C to 45°C, with fitted temperature sensitivities of 68 pm/°C for λ_+ and 70 pm/°C for λ_- . In contrast, the $\Delta\lambda_s$ changes by only -1.6 pm/°C—approximately 43-fold smaller than the individual shifts. This pronounced disparity indicates that mode splitting readout effectively suppresses temperature-induced fluctuations, ensuring stable sensor operation under practical conditions. Overall, these analyses substantiate $\Delta\lambda_s$ as an intrinsically bulk-insensitive and environmentally robust spectral indicator, underscoring its potential for high-stability surface-sensing applications.

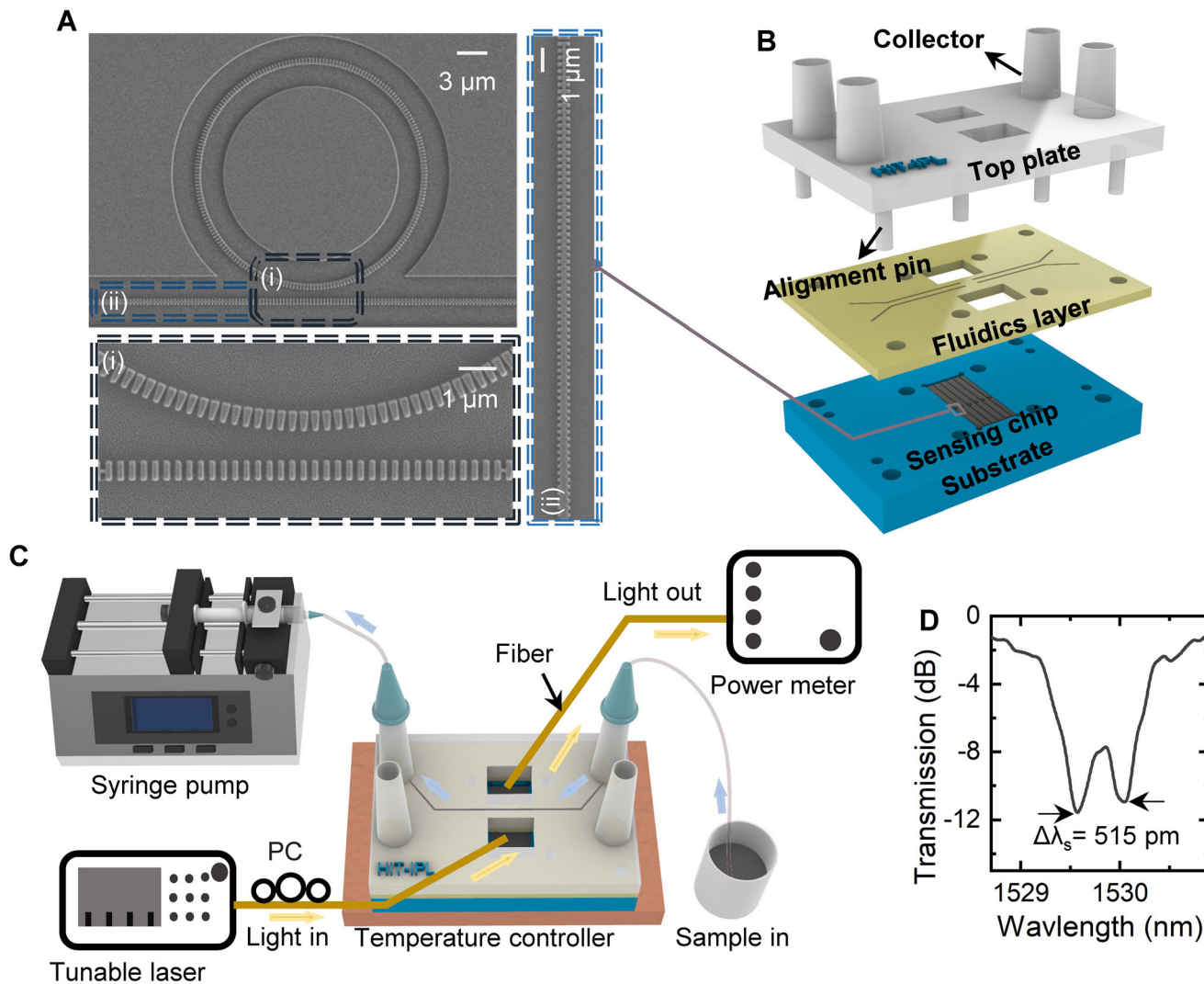


FIGURE 3 | Fabricated MWMR device and experimental setup. (A) SEM images of the fabricated MWMR: (i) coupling region and (ii) adiabatic mode converter (ring radius = 10 μm). (B) Customized microfluidic system. (C) Automated optical testing platform. (D) Transmission spectrum of the MWMR exhibiting mode splitting when immersed in PBS buffer.

2.3 | Detection of Ultra-Weak Surface Perturbation

The ability of mode splitting-based MWMRs to resolve interfacial ultra-weak perturbations is validated using the streptavidin–biotin interaction as a representative model system. In this experiment, the binding process provides a controlled and quantifiable refractive index variation at the waveguide surface, enabling systematic assessment of the platform’s detection capability. The surface functionalization procedure, illustrated in Figure 5A, involved immobilizing 10 mg/mL Sulfo-NHS-Biotin onto the APTES layer, followed by blocking with 1% BSA to prevent non-specific binding (details in the Materials and Methods). High-concentration probe and blocking solutions are used to maximize the probe coverage of the sensor surface. The signals harvested during the initial PBS wash serve as the baseline for subsequent measurements. Figure 5B summarizes the spectral responses throughout the entire surface functionalization procedure. Spectra at equilibrium states T1 (baseline), T2 (after Sulfo-NHS-Biotin immobilization followed by PBS washing), and

T3 (after BSA blocking followed by PBS washing) illustrate the evolution of mode splitting, as shown in the inset of Figure 5B. $\Delta\lambda_s$ at these states are 476.9 pm, 511.2 pm, and 514.7 pm, respectively.

Following functionalization, various concentrations of streptavidin solutions are measured sequentially, with PBS flowing after each step to remove unbound streptavidin molecules. Figure 6A shows the temporal trace of $\Delta\lambda_s$ extracted from over 850 spectra. The equilibrium spectra at T3 (after BSA blocking and PBS washing), T_A (after the injection of 0.01 pg/mL streptavidin followed by PBS washing), and T_B (after the injection of 0.1 pg/mL streptavidin followed by PBS washing) illustrate the evolution of mode splitting, as shown in the insets of Figure 6A (additional concentration responses can be found in Section S8 and Figure S5). The corresponding time-dependent mode splitting $\Delta\lambda_s(t)$ at different equilibrium states is provided in Section S9 and Figure S6). Using the averaged initial mode splitting value of 515.97 pm as the baseline, Figure 6B summarizes the quantified responses of λ_+ , λ_- , and $\Delta\lambda_s$ to two ultra-low concentrations of streptavidin. Blue shifts of individual resonance (λ_+ or λ_-) are observed at

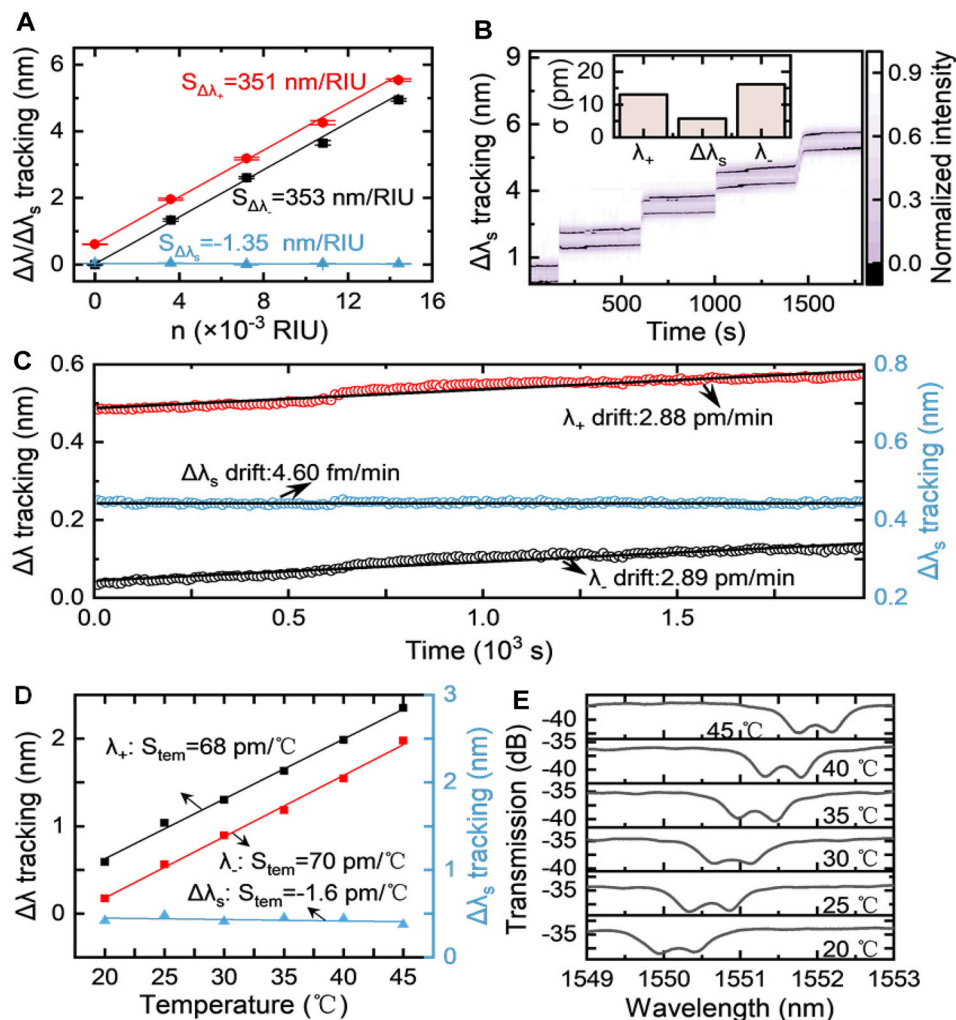


FIGURE 4 | Sensing performance and stability of the mode splitting-based MWMR. (A) Experimental bulk refractometric sensitivities of λ_+ , λ_- , and $\Delta\lambda_s$. (B) Normalized spectral responses of λ_+ , λ_- , and $\Delta\lambda_s$ under bulk-index perturbations; inset compares their baseline noise levels (standard deviation). (C) Baseline drift monitoring in PBS after APTES modification. (D) Temperature sensitivities of λ_+ , λ_- , and $\Delta\lambda_s$. (E) Transmission spectra at different stage temperatures.

both concentrations, indicating that the detectable range for the wavelength shift-based interrogation method exceeds 0.1 pg/mL, as shown in inset (i) of Figure 6B. The observed blue shifts in λ_+ and λ_- are likely attributed to probe detachments and/or silicon etching in biological solutions, as suggested by recent studies [39]. In contrast to resonance wavelength shifts, fluctuations in mode splitting are considerably weaker during measurement, since mode splitting depends on changes in the reflectivity of the meta-grating induced by the accumulation of biomolecules rather than variations in the effective index of the modes within the ring [24]. As shown in inset (ii) of Figure 6B, the σ of $\Delta\lambda_s$ (1.3 pm) is reduced by more than threefold compared to the individual wavelength deviations of λ_+ (4.1 pm) and λ_- (4.07 pm). $\Delta\lambda_s$ decreases by 2.74 pm upon applying 0.01 pg/mL streptavidin, indicating that the MWMR can detect streptavidin at this ultra-low concentration, as shown in Figure 6B. For 0.1 pg/mL streptavidin, $\Delta\lambda_s$ further decreased by 2.22 pm. Compared with the detectable concentration achieved by the wavelength-shift approach (higher than 0.1 pg/mL), the mode splitting scheme reduces the detectable concentration by at least two orders of magnitude. This improvement arises from

the discernible yet stable mode splitting response to interfacial refractive-index perturbations, whereas its negligible sensitivity to homogeneous background variations ensures reliable identification of surface-binding events. It should be noted that the mode splitting-based interrogation is intrinsically nonlinear, with concentration-dependent sensitivity governed by the underlying mode-coupling dynamics. As a result, the response is not intended to be strictly linear over a broad range, but instead optimized for detecting subtle perturbations in the ultra-low-concentration regime relevant to lethal pathogens (see Section S10 and Figure S7).

3 | Discussion

This study demonstrates that harnessing residual reflection in MWMRs enables mode splitting to serve as a self-referenced architecture for surface refractive-index sensing. Unlike conventional wavelength-shift interrogation, which is highly susceptible to baseline drift and environmental fluctuations and often fails to resolve ultra-weak surface perturbations, mode splitting

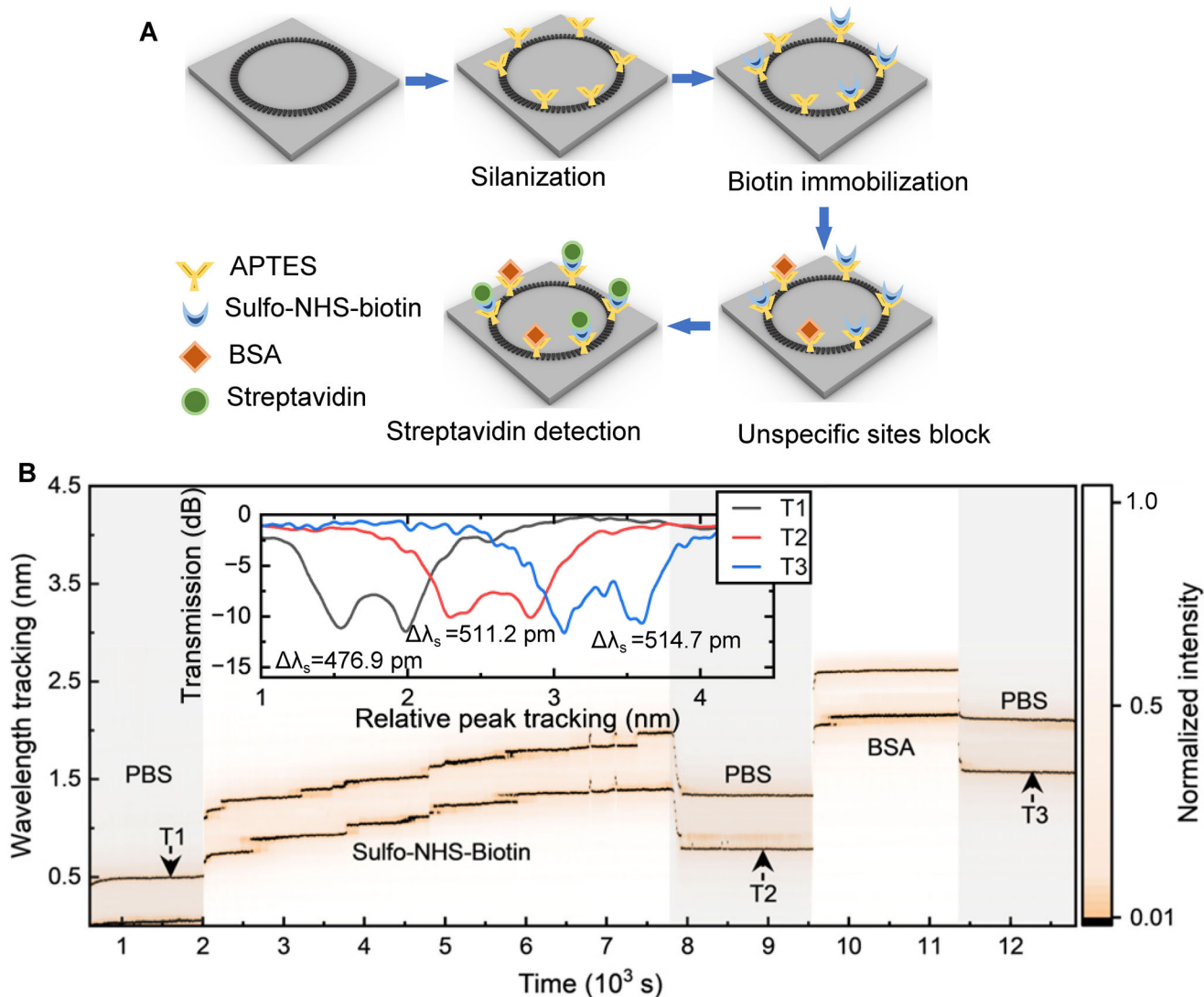


FIGURE 5 | Surface functionalization responses of the mode splitting-based MWMR. (A) Schematic illustration of surface functionalization, including Sulfo-NHS-Biotin immobilization, BSA blocking, and subsequent streptavidin detection. (B) Normalized spectral responses of the splitting modes during Sulfo-NHS-Biotin immobilization and BSA blocking. Insets show mode splitting spectra at equilibrium states T1 (baseline), T2 (after Sulfo-NHS-Biotin immobilization followed by PBS washing), and T3 (after BSA blocking followed by PBS washing).

exhibits intrinsic stability and strong immunity to noise owing to its differential nature. Experimentally, mode splitting shows an exceptionally low baseline drift of only 4.6 fm/min. Its modest temperature sensitivity (-1.6 pm/ $^{\circ}$ C) further confirms robust operation without stringent temperature control. Interfacial refractive-index perturbations modulate the reflection and consequently alter $\Delta\lambda_s$, allowing quantitative yet noise-resilient interrogation of surface processes. The streptavidin–biotin assay corroborates this mechanism, revealing discernible splitting variations upon molecular binding and confirming a detection limit of 0.01 pg/mL with a splitting noise of 1.3 pm. These results validate that reflection-induced mode splitting effectively decouples surface-specific responses from bulk and environmental disturbances, enabling reliable identification of ultra-weak interfacial events.

Table 1 summarizes surface sensing performance reported for various microring-based structures. Wavelength-shift-based

strip microrings generally exhibit detection limits within the pg/mL to ng/mL range (Refs [6, 7]), while pedestal-type MWMRs further improve structural sensitivity, reaching 0.1 ng/mL [17]. Compared to sensors based on wavelength shift, mode splitting-based MWMRs achieve 2–5 orders of magnitude improvement in detectable concentrations. Additionally, compared with other mode-splitting-based sensors such as Bragg-grating microrings for rhS100A4 [24] and EP-based sensors for single-particle detection [42], the mode splitting-based MWMR achieves substantially improved detection performance while maintaining strong noise immunity. As noted in Ref. [38], achieving a low LOD in biosensing requires minimizing both baseline drift and noise, with Biacore defining LOD as (baseline drift + $3 \times$ noise standard deviation). The mode splitting-based MWMR intrinsically satisfies this requirement through its self-referenced optical splitting mechanism, effectively reducing both baseline drift and bioprocess-induced fluctuations.

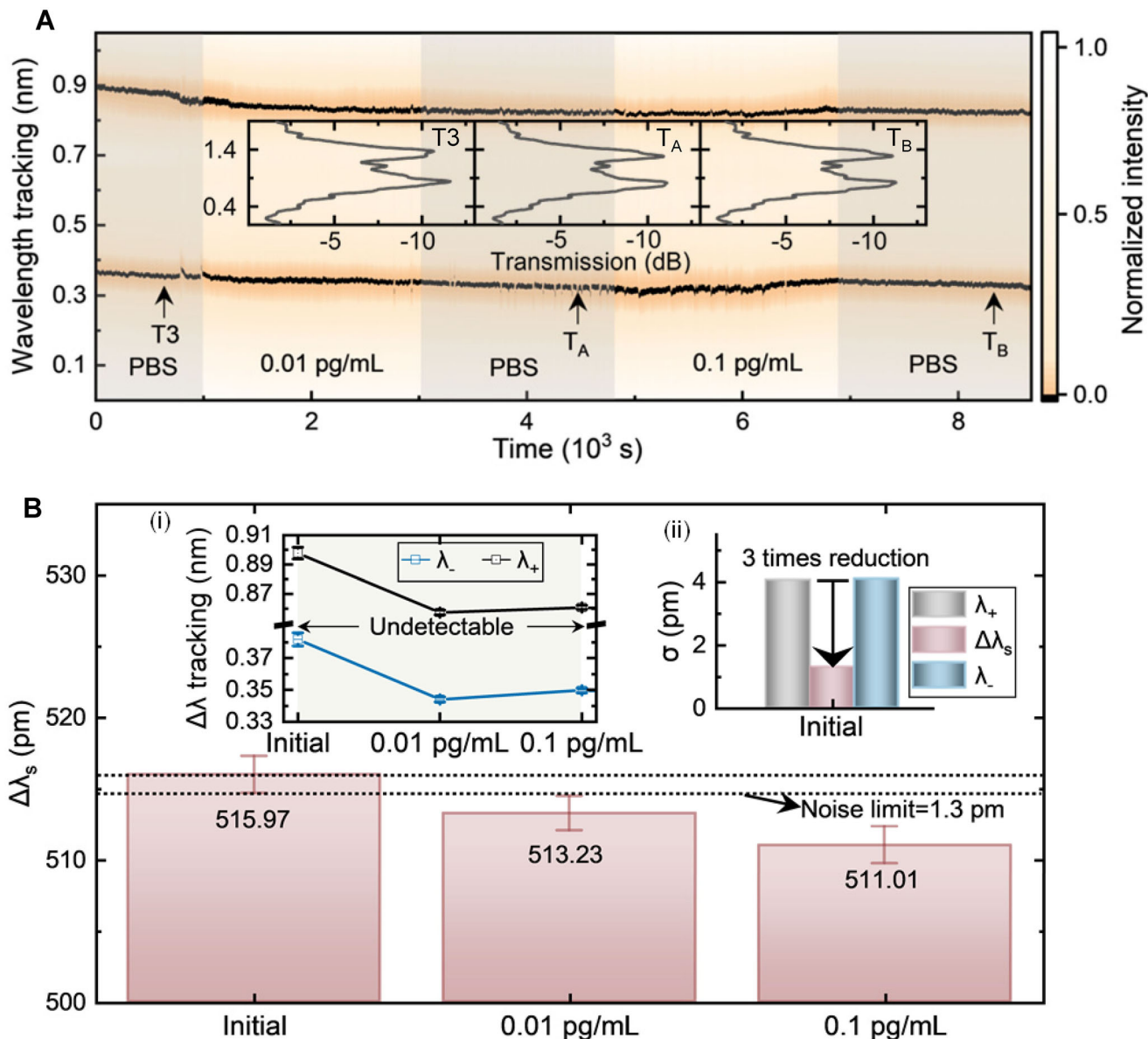


FIGURE 6 | Ultra-low-concentration streptavidin detection. (A) Temporal trace of $\Delta\lambda_s$ extracted from sequential measurements of streptavidin at different concentrations with PBS washing. Insets show equilibrium mode splitting spectra at T3 (after BSA blocking and PBS washing), T_A (after 0.01 pg/mL streptavidin injection and PBS washing), and T_B (after 0.01 pg/mL streptavidin injection and PBS washing). (B) Quantified responses of λ_+ , λ_- , and $\Delta\lambda_s$ at different streptavidin concentrations. Insets: (i) individual resonance blue shifts of λ_+ and λ_- ; (ii) baseline noise comparison among λ_+ , λ_- , and $\Delta\lambda_s$.

These attributes make the mode-splitting-based MWMR architecture particularly advantageous for sensing scenarios demanding simultaneous high sensitivity and noise robustness. Beyond the demonstrated streptavidin–biotin assay, this platform could be readily extended to nanoscale biological targets such as extracellular vesicles, which play pivotal roles in immune regulation, coagulation, and intercellular communication [45–47]. The broader extensibility of this platform is also supported by recent demonstrations of meta-ring resonators on the SiN platform [48]. Collectively, these results establish reflection-induced mode splitting as a powerful photonic mechanism that enables drift-immune, trace-level detection, positioning MWMRs as a high-performance and broadly applicable platform for precision surface refractometric sensing.

4 | Materials and Methods

4.1 | Fabrication of the MWMR

The structures are fabricated on a silicon-on-insulator (SOI) wafer, consisting of a 220-nm-thick single-crystal silicon layer separated from the silicon handle wafer by a 2- μ m-thick buried oxide (SiO₂) layer. The diluted ZEP520A resist is spin-coated on a Piranha-cleaned chip and baked at 180°C for 20 min before E-beam lithography (NanoBeam, nB5) to ensure successful nanostructure fabrication. The designs are then transferred to the silicon layer using inductively coupled plasma (ICP) etching. A 10-nm-thick silica layer is deposited on the MWMRs via plasma-enhanced chemical vapor deposition (PECVD) to

TABLE 1 | The sensing performance of microring-based sensors.

Structure	Method	Analyte	Achieved detectable concentration	Ref
Cascaded microring	Wavelength shift	HSA	18.09 ng/mL	[6]
Strip microring	Wavelength shift	Streptavidin	~60 fM ^a (estimate value~3.59 pg/mL)	[7]
MWMR	Wavelength shift	Streptavidin	10 µg/mL	[43]
Pedestal-MWMR	Wavelength shift	Streptavidin	0.1 ng/mL	[17]
Bragg-gating-based microring	Mode splitting	rhS100A4	1 µM	[24]
EP-based microring	Mode splitting	Polystyrene nanoparticles	20 fM ^b	[42]
This work (mode splitting-based MWMRs)	Mode splitting	Streptavidin	0.01 pg/mL (~0.167 fM)	

^aThe strip microring with an estimated detectable concentration of 3.59 pg/mL, attributed to its superior relative spectral resolution and an extremely low noise limit of 0.31 pm (3σ), achieved through simultaneous sweeping with a 25-GHz Fabry-Perot etalon.

^bThe EP-based microring is used for detecting polystyrene (PS) particles, with the concentration recorded here referring specifically to the concentration of PS particle solutions.

protect the device from bioassays and enhance salinization performance.

4.2 | Surface Functionalization and Sample Preparations

A self-assembled monolayer of 3-Aminopropyl triethoxysilane (APTES) is formed on the surface of the MWMR, providing amine groups ($-\text{NH}_2$) for binding probe proteins. The chip is baked at 120°C for 1 h under ambient conditions to enhance the stability of the functional groups. After APTES modification, 10 mg/mL Sulfo-NHS-Biotin (Sigma-Aldrich), a receptor of streptavidin, is flowed to the APTES/MWMR through the microfluidic channel by syringe pump with a pumping speed of 50 µL/min for 1 h. After immobilizing the probes, the remaining chip surface is blocked with 1% BSA in PBS to minimize non-specific binding. The standard streptavidin (SA) powder (Sigma-Aldrich) is prepared into 0.01 pg/mL, 0.1 pg/mL, 1 pg/mL, 10 pg/mL, and 100 pg/mL in a solution of PBS for studying the sensitivity of the mode splitting-based MWMRs.

4.3 | Microfluidic System

The microfluidic system is illustrated in Figure 3B, which employs a sandwich structure for encapsulation, composed of a top plate, a fluidics layer, and a substrate plate with a rectangular pocket for holding a chip in place. The sample sources are injected into the microfluidic channel from the inflow tube. A syringe for pumping the biomolecules is connected to the outflow tube by a stepping motor to control the flow rate. The standard Luer taper is integrated with the collector for fluid flow in the circuit.

4.4 | Automatic Testing System

Light from a tunable laser (Santec TSL550), controlled by a polarization controller, is coupled into and out of the chip using

grating couplers (more details can be found in Section S11 and Figure S8). The stage temperature is controlled at 25°C with an Apico (AP-TEC-PRO) temperature controller to avoid thermal effect-induced resonance shift during biosensing testing. The transmission spectra are monitored by the optical power meter (Santec MPM-210H).

Acknowledgements

This research is supported by the National Natural Science Foundation of China (NSFC) (U22A2093); Science, Technology and Innovation Commission of Shenzhen Municipality (GXWD20231130113557001; JCYJ20210324131614040).

Conflicts of Interest

The authors declare no conflict of interest.

Data Availability Statement

The data that support the findings of this study are available on request from the corresponding author.

References

- J.-F. Masson, "Ultralow Concentration Sensing: What Should We be Aware Of?," *ACS Sensors* 8 (2023): 941–942, <https://doi.org/10.1021/acssensors.3c00396>.
- A. G. González and M. Á. Herrador, "A Practical Guide to Analytical Method Validation, Including Measurement Uncertainty and Accuracy Profiles," *TrAC Trends in Analytical Chemistry* 26 (2007): 227–238, <https://doi.org/10.1016/j.trac.2007.01.009>.
- S. Wu, Y. Guo, W. Wang, J. Zhou, and Q. Zhang, "Label-Free Biosensing Using a Microring Resonator Integrated with Poly-(dimethylsiloxane) Microfluidic Channels," *Review of Scientific Instruments* 90 (2019): 035004, <https://doi.org/10.1063/1.5074134>.
- Y. Chen, F. Yu, C. Yang, et al., "Label-Free Biosensing Using Cascaded Double-Microring Resonators Integrated with Microfluidic Channels," *Optics Communications* 344 (2015): 129–133, <https://doi.org/10.1016/j.optcom.2015.01.028>.

5. X. Chen, M. Li, Z. Wang, et al., "A Label-Free Optical Biosensor Based on an Array of Microring Resonators for the Detection of Human Serum Albumin," *Sensors* 24 (2024): 677, <https://doi.org/10.3390/s24020677>.
6. Z. Wang, M. Li, X. Chen, et al., "Temperature-Insensitive Cascaded Micro-Ring Resonator Silicon Photoelectric Sensor Based on Wavelength Interrogation for HSA Detection," *Sensors and Actuators B: Chemical* 408 (2024): 135512, <https://doi.org/10.1016/j.snb.2024.135512>.
7. M. Iqbal, M. A. Gleeson, B. Spaugh, et al., "Label-Free Biosensor Arrays Based on Silicon Ring Resonators and High-Speed Optical Scanning Instrumentation," *IEEE Journal of Selected Topics in Quantum Electronics* 16 (2010): 654–661, <https://doi.org/10.1109/JSTQE.2009.2032510>.
8. A. J. Qavi, K. Meserve, M. J. Aman, et al., "Rapid Detection of an Ebola Biomarker with Optical Microring Resonators," *Cell Reports Methods* 2 (2022): 100234, <https://doi.org/10.1016/j.crmeth.2022.100234>.
9. F. Vollmer and L. Yang, "Review Label-Free Detection with High-Q Microcavities: A Review of Biosensing Mechanisms for Integrated Devices," *Nanophotonics* 1 (2012): 267–291, <https://doi.org/10.1515/nanoph-2012-0021>.
10. W. Zhang, S. Serna, X. Le Roux, L. Vivien, and E. Cassan, "Highly Sensitive Refractive Index Sensing by Fast Detuning the Critical Coupling Condition of Slot Waveguide Ring Resonators," *Optics Letters* 41 (2016): 532–535, <https://doi.org/10.1364/OL.41.000532>.
11. C. Y. Zhao, L. Zhang, and C. M. Zhang, "Compact SOI Optimized Slot Microring Coupled Phase-Shifted Bragg Grating Resonator for Sensing," *Optics Communications* 414 (2018): 212–216, <https://doi.org/10.1016/j.optcom.2018.01.010>.
12. D. Urbonas, A. Balcytis, K. Vaskevicius, M. Gabalis, and R. Petruskevicius, "Air and Dielectric Bands Photonic Crystal Microring Resonator for Refractive Index Sensing," *Optics Letters* 41 (2016): 3655–3658, <https://doi.org/10.1364/OL.41.003655>.
13. S. M. Lo, S. Hu, G. Gaur, Y. Kostoulas, S. M. Weiss, and P. M. Fauchet, "Photonic Crystal Microring Resonator for Label-Free Biosensing," *Optics Express* 25 (2017): 7046–7054, <https://doi.org/10.1364/OE.25.007046>.
14. V. Donzella, A. Sherwali, J. Flueckiger, S. M. Grist, S. T. Fard, and L. Chrostowski, "Design and Fabrication of SOI Micro-Ring Resonators Based on Sub-Wavelength Grating Waveguides," *Optics Express* 23 (2015): 4791–4803, <https://doi.org/10.1364/OE.23.004791>.
15. H. Yan, L. Huang, X. Xu, et al., "Unique Surface Sensing Property and Enhanced Sensitivity in Microring Resonator Biosensors Based on Sub-wavelength Grating Waveguides," *Optics Express* 24 (2016): 29724–29733, <https://doi.org/10.1364/OE.24.029724>.
16. Z. Wang, X. Xu, D. Fan, Y. Wang, and R. T. Chen, "High Quality Factor Subwavelength Grating Waveguide Micro-Ring Resonator Based on Trapezoidal Silicon Pillars," *Optics Letters* 41 (2016): 3375–3378, <https://doi.org/10.1364/OL.41.003375>.
17. C. W. Chang, X. Xu, S. Chakravarty, et al., "Pedestal Subwavelength Grating Metamaterial Waveguide Ring Resonator for Ultra-Sensitive Label-Free Biosensing," *Biosensors and Bioelectronics* 141 (2019): 111396, <https://doi.org/10.1016/j.bios.2019.111396>.
18. G. Besselink, R. Heideman, E. Schreuder, L. Wevers, F. Falke, and H. Van den Vlekert, "Performance of Arrayed Microring Resonator Sensors with the TriPleX Platform," *Journal of Biosensors & Bioelectronics* 7 (2016): 1000209, <http://doi.org/10.4172/2155-6210.1000209>.
19. B. E. Little, J.-P. Laine, and S. T. Chu, "Surface-Roughness-Induced Contradirectional Coupling in Ring and Disk Resonators," *Optics Letters* 22 (1997): 4–6, <https://doi.org/10.1364/OL.22.000004>.
20. J. Zhu, S. K. Ozdemir, Y.-F. Xiao, et al., "On-Chip Single Nanoparticle Detection and Sizing by Mode Splitting in an Ultrahigh-Q Microresonator," *Nature Photonics* 4 (2009): 46–49, <https://doi.org/10.1038/nphoton.2009.237>.
21. Y. Chen, J. Duan, J. Li, X. Xu, and J. Wang, "High-Order Autler-Townes Splitting in Electrically Tunable Photonic Molecules," *Photonics Research* 12 (2024): 1794–1801, <https://doi.org/10.1364/PRJ.52-5601>.
22. J. Li, W. Li, Y. Feng, et al., "On-Chip Fabrication-Tolerant Exceptional Points Based on Dual-Scatterer Engineering," *Nano Letters* 24 (2024): 3906–3913, <https://doi.org/10.1021/acs.nanolett.3c05075>.
23. W. Li, J. Li, L. Yu, et al., "Observation of Autler-Townes Splitting in Subwavelength Grating Metamaterial Ring Resonators," *APL Photonics* 8 (2023): 016102, <https://doi.org/10.1063/5.0122472>.
24. M. de Goede, M. Dijkstra, L. Chang, et al., "Mode-Splitting in a Microring Resonator for Self-Referenced Biosensing," *Optics Express* 29 (2021): 346–358, <https://doi.org/10.1364/OE.411931>.
25. N. Acharyya, M. Maher, and G. Kozyreff, "Portable Microresonator-Based Label-Free Detector: Monotonous Resonance Splitting with Particle Adsorption," *Optics Express* 27 (2019): 34997–35011, <https://doi.org/10.1364/OE.27.034997>.
26. X. Lu, A. Rao, G. Moille, D. A. Westly, and K. Srinivasan, "Universal Frequency Engineering Tool for Microcavity Nonlinear Optics: Multiple Selective Mode Splitting of Whispering-Gallery Resonances," *Photonics Research* 8 (2020): 1676–1686, <https://doi.org/10.1364/PRJ.401755>.
27. X. Lu, S. Rogers, W. C. Jiang, and Q. Lin, "Selective Engineering of Cavity Resonance for Frequency Matching in Optical Parametric Processes," *Applied Physics Letters* 105 (2014): 151104, <https://doi.org/10.1063/1.4898001>.
28. S. Gafsi and J. D. Ryckman, "All-Dielectric Metawaveguide Ring Resonators with Deeply Sub-Diffractive Mode Volumes," *Laser & Photonics Reviews* 19 (2025): 2401579, <https://doi.org/10.1002/lpor.202401579>.
29. L. He, Ş. K. Özdemir, J. Zhu, W. Kim, and L. Yang, "Detecting Single Viruses and Nanoparticles Using Whispering Gallery Microlasers," *Nature Nanotechnology* 6 (2011): 428–432, <https://doi.org/10.1038/nnano.2011.99>.
30. P. Cheben, R. Halir, J. H. Schmid, H. A. Atwater, and D. R. Smith, "Subwavelength Integrated Photonics," *Nature* 560 (2018): 565–572, <https://doi.org/10.1038/s41586-018-0421-7>.
31. Z. Tu, D. Gao, M. Zhang, and D. Zhang, "High-Sensitivity Complex Refractive Index Sensing Based on Fano Resonance in the Subwavelength Grating Waveguide Micro-Ring Resonator," *Optics Express* 25 (2017): 20911–20922, <https://doi.org/10.1364/OE.25.020911>.
32. B. E. A. Saleh and M. C. Teich, *Fundamentals of Photonics*, 3rd ed. (John Wiley & Sons, Hoboken, New Jersey, 2019).
33. R. D. Meade, J. N. Winn, and J. Joannopoulos, *Photonic Crystals: Molding the Flow of Light* (Princeton Press, Princeton, New Jersey, 1995).
34. R. Cheng, Y. Han, and L. Chrostowski, "Characterization and Compensation of Apodization Phase Noise in Silicon Integrated Bragg Gratings," *Optics Express* 27 (2019): 9516–9535, <https://doi.org/10.1364/OE.27.009516>.
35. N. Skivesen, A. Têtu, M. Kristensen, J. Kjems, L. H. Frandsen, and P. I. Borel, "Photonic-Crystal Waveguide Biosensor," *Optics Express* 15 (2007): 3169–3176, <https://doi.org/10.1364/OE.15.003169>.
36. A. K. Mudraboyina and J. Sabarinathan, "Protein Binding Detection Using On-Chip Silicon Gratings," *Sensors* 11 (2011): 11295–11304, <https://doi.org/10.3390/s111211295>.
37. Y. Hu, L. Shao, S. Arnold, Y.-C. Liu, C.-Y. Ma, and Y.-F. Xiao, "Mode Broadening Induced by Nanoparticles in an Optical Whispering-Gallery Microcavity," *Physical Review A* 90 (2014): 043847, <https://doi.org/10.1103/PhysRevA.90.043847>.
38. T. Yang, S. Chen, X. He, H. Guo, and X. Sun, "How to Convincingly Measure Low Concentration Samples with Optical Label-Free Biosensors," *Sensors and Actuators B: Chemical* 306 (2020): 127568, <https://doi.org/10.1016/j.snb.2019.127568>.

39. Cytiva, "Biacore 1 Series SPR Systems," accessed April 14, 2026, available at: <https://www.cytivalifesciences.com/en/us/shop/protein-analysis/spr-label-free-analysis/spr-systems/biacore-1-series-spr-systems-p-57220>.
40. J. Komma, C. Schwarz, G. Hofmann, D. Heinert, and R. Nawrodt, "Thermo-Optic Coefficient of Silicon at 1550 nm and Cryogenic Temperatures," *Applied Physics Letters* 101 (2012): 041905, <https://doi.org/10.1063/1.4738989>.
41. G. J. Triggs, G. J. Evans, and T. F. Krauss, "Degradation of Silicon Photonic Biosensors in Cell Culture Media: Analysis and Prevention," *Biomedical Optics Express* 8 (2017): 2924–2931, <http://doi.org/10.1364/BOE.8.002924>.
42. W. Chen, S. K. Ozdemir, G. Zhao, J. Wiersig, and L. Yang, "Exceptional Points Enhance Sensing in an Optical Microcavity," *Nature* 548 (2017): 192–196, <https://doi.org/10.1038/nature23281>.
43. V. Soni, C.-W. Chang, X. Xu, et al., "Portable Automatic Microring Resonator System Using a Subwavelength Grating Metamaterial Waveguide for High-Sensitivity Real-Time Optical-Biosensing Applications," *IEEE Transactions on Biomedical Engineering* 68 (2020): 1894–1902, <https://doi.org/10.1109/TBME.2020.3029148>.
44. A. Famil'tseva, N. Jeremic, and S. C. J. M. Tyagi, "Exosomes: Cell-Created Drug Delivery Systems," *Molecular and Cellular Biochemistry* 459 (2019): 1–6, <https://doi.org/10.1007/s11010-019-03545-4>.
45. E. Serrano-Pertierra, M. Oliveira-Rodríguez, M. Matos, et al., "Extracellular Vesicles: Current Analytical Techniques for Detection and Quantification," *Biomolecules* 10 (2020): 824, <https://doi.org/10.3390/biom10060824>.
46. J. Wang, X. Huang, J. Xie, Y. Han, Y. Huang, and H. Zhang, "Exosomal Analysis: Advances in Biosensor Technology," *Clinica Chimica Acta* 518 (2021): 142–150, <https://doi.org/10.1016/j.cca.2021.03.026>.
47. S. Tabassum and S. Aryal, "Real-time quantification of CD63 with anti-CD63 functionalized plasmonic fiber optic probe," *Proc. SPIE* 11953, San Francisco, CA, (2022): 1195304.
48. C. M. Naraine, J. N. Westwood-Bachman, C. Horvath, et al., "Subwavelength Grating Metamaterial Waveguides and Ring Resonators on a Silicon Nitride Platform," *Laser & Photonics Reviews* 17 (2023): 2200216, <https://doi.org/10.1002/lpor.202200216>.
49. X. Xu, H. Subbaraman, J. Covey, D. Kwong, A. Hosseini, and R. T. Chen, "Complementary Metal–Oxide–Semiconductor Compatible High Efficiency Subwavelength Grating Couplers for Silicon Integrated Photonics," *Applied Physics Letters* 101 (2012): 031109, <https://doi.org/10.1063/1.4737412>.

Supporting Information

Additional supporting information can be found online in the Supporting Information section.

Supporting File: advs75339-sup-0001-SupMat.docx.